

# The first day of the Cenozoic

Sean P. S. Gulick<sup>a,b,1</sup>, Timothy J. Bralower<sup>c</sup>, Jens Ormö<sup>d</sup>, Brendon Hall<sup>e</sup>, Kliti Grice<sup>f</sup>, Bettina Schaefer<sup>f</sup>, Shelby Lyons<sup>c</sup>, Katherine H. Freeman<sup>c</sup>, Joanna V. Morgan<sup>g</sup>, Natalia Artemieva<sup>h</sup>, Pim Kaskes<sup>i</sup>, Sietze J. de Graaff<sup>i</sup>, Michael T. Whalen<sup>j</sup>, Gareth S. Collins<sup>g</sup>, Sonia M. Tikoo<sup>k</sup>, Christina Verhagen<sup>k</sup>, Gail L. Christeson<sup>a</sup>, Philippe Claeys<sup>i</sup>, Marco J. L. Coolen<sup>f</sup>, Steven Goderis<sup>i</sup>, Kazuhisa Goto<sup>l</sup>, Richard A. F. Grieve<sup>m</sup>, Naoma McCall<sup>a,b</sup>, Gordon R. Osinski<sup>m</sup>, Auriol S. P. Rae<sup>g</sup>, Ulrich Riller<sup>n</sup>, Jan Smit<sup>o</sup>, Vivi Vajda<sup>p</sup>, Axel Wittmann<sup>q</sup>, and the Expedition 364 Scientists<sup>2</sup>

<sup>a</sup>Institute for Geophysics, Jackson School of Geosciences, University of Texas at Austin, Austin, TX 78758; <sup>b</sup>Department of Geological Sciences, Jackson School of Geosciences, University of Texas at Austin, Austin, TX 79712; <sup>c</sup>Department of Geosciences, Pennsylvania State University, University Park, PA 16801; <sup>d</sup>Centro de Astrobiología Instituto Nacional de Técnica Aeroespacial-Spanish National Research Council (INTA-CSIC), Instituto Nacional de Técnica Aeroespacial, 28850 Torrejón de Ardoz, Spain; <sup>e</sup>Enthought, Inc., Austin, TX 78701; <sup>f</sup>Western Australian Organic and Isotope Geochemistry Centre, The Institute for Geoscience Research, School of Earth and Planetary Science, Curtin University, Perth, WA 6102, Australia; <sup>g</sup>Department of Earth Science and Engineering, Imperial College London, SW7 2AZ London, United Kingdom; <sup>h</sup>Planetary Science Institute, Tucson, AZ 85719-2395; <sup>i</sup>Analytical, Environmental and Geo-Chemistry, Vrije Universiteit Brussel, Pleinlaan 2, B-1050 Brussels, Belgium; <sup>j</sup>Department of Geosciences, University of Alaska Fairbanks, Fairbanks, AK 99775; <sup>k</sup>Department of Earth and Planetary Sciences, Rutgers University, New Brunswick, NJ 08854; <sup>l</sup>International Research Institute of Disaster Science, Tohoku University, Sendai 980-8572, Japan; <sup>m</sup>Department of Earth Sciences, University of Western Ontario, London, ON, N6A 3K7, Canada; <sup>n</sup>Institut für Geologie, Universität Hamburg, 20146 Hamburg, Germany; <sup>o</sup>Faculty of Earth and Life Sciences (FALW), Vrije Universiteit Amsterdam, 1081 HV, Amsterdam, The Netherlands; <sup>p</sup>Swedish Museum of Natural History, 114 18 Stockholm, Sweden; and <sup>q</sup>Eyring Materials Center, Arizona State University, Tempe, AZ 85287-1704

Edited by Michael Manga, University of California, Berkeley, CA, and approved July 30, 2019 (received for review June 5, 2019)

**Highly expanded Cretaceous–Paleogene (K–Pg) boundary section from the Chicxulub peak ring, recovered by International Ocean Discovery Program (IODP)–International Continental Scientific Drilling Program (ICDP) Expedition 364, provides an unprecedented window into the immediate aftermath of the impact. Site M0077 includes ~130 m of impact melt rock and suevite deposited the first day of the Cenozoic covered by <1 m of micrite-rich carbonate deposited over subsequent weeks to years. We present an interpreted series of events based on analyses of these drill cores. Within minutes of the impact, centrally uplifted basement rock collapsed outward to form a peak ring capped in melt rock. Within tens of minutes, the peak ring was covered in ~40 m of brecciated impact melt rock and coarse-grained suevite, including clasts possibly generated by melt–water interactions during ocean resurge. Within an hour, resurge crested the peak ring, depositing a 10-m-thick layer of suevite with increased particle roundness and sorting. Within hours, the full resurge deposit formed through settling and seiches, resulting in an 80-m-thick fining-upward, sorted suevite in the flooded crater. Within a day, the reflected rim-wave tsunami reached the crater, depositing a cross-bedded sand-to-fine gravel layer enriched in polycyclic aromatic hydrocarbons overlain by charcoal fragments. Generation of a deep crater open to the ocean allowed rapid flooding and sediment accumulation rates among the highest known in the geologic record. The high-resolution section provides insight into the impact environmental effects, including charcoal as evidence for impact-induced wildfires and a paucity of sulfur-rich evaporites from the target supporting rapid global cooling and darkness as extinction mechanisms.**

Chicxulub impact crater | suevite | Cretaceous–Paleogene | peak ring | tsunami

Impacts of asteroids and comets are a dominant geologic process on rocky planets (1). The largest impact structures—peak ring craters and multiring impact basins—exhibit annular rings of elevated topography surrounding their centers called peak rings. In 2016, a peak ring was drilled for the first time at the ~200-km-diameter Chicxulub impact structure (Fig. 1) during International Ocean Discovery Program (IODP)–International Continental Scientific Drilling Program (ICDP) Expedition 364 (2, 3). Drill core showed that the bulk of the Chicxulub peak ring was formed from uplifted, fractured, and shocked granitic rocks with unusually low density and seismic velocity cross-cut by magmatic sheet intrusions and shear zones (2, 4). These results support the dynamic collapse model for peak ring formation (5), in which rocks temporarily flow like a viscous fluid, moving inward and upward to

form a zone of central uplift and then, collapse outward and downward to form a peak ring (6). Within tens of seconds of the impact, a ~40- to 50-km-radius transient cavity was formed (Fig. 2 A and B) and lined with impact melt (5). The main mass of this melt ends up inside the peak ring, forming the central impact melt sheet (Fig. 2), but some melt drapes and covers the peak ring and extends into the annular trough (7–9).

Impact cratering is an extremely energetic process that results in the formation of a variety of breccia layers within and outside craters. One of the characteristic impact breccias is a polymict melt-bearing breccia, informally termed suevite, that contains shocked clasts (10–12). Emplacement mechanisms for suevite vary among and within craters and with marine and nonmarine settings (13–20). Additionally, the sources of the material in these impactites are debated (21). For instance, occurrences of suevite have been attributed to a melt-rich flow from the overshooting central uplift during crater collapse

## Significance

**Chicxulub impact crater cores from the peak ring include ~130 m of impact melt rock and breccia deposited on the first day of the Cenozoic. Within minutes of the impact, fluidized basement rocks formed a ring of hills, which were rapidly covered by ~40 m of impact melt and breccia. Within an hour, ocean waters flooded the deep crater through a northeast embayment, depositing another 90 m of breccia. Within a day, a tsunami deposited material from distant shorelines, including charcoal. Charcoal and absence of sulfur-rich target rocks support the importance of impact-generated fires and release of sulfate aerosols for global cooling and darkness postimpact.**

Author contributions: S.P.S.G., J.V.M., and G.L.C. designed research; S.P.S.G., T.J.B., J.O., B.H., K. Grice, B.S., S.L., K.H.F., J.V.M., N.A., P.K., S.J.d.G., M.T.W., G.S.C., S.M.T., C.V., G.L.C., P.C., M.J.L.C., S.G., K. Goto, N.M., G.R.O., A.S.P.R., U.R., J.S., V.V., A.W., and E.364.S. performed research; S.P.S.G., T.J.B., J.O., K. Grice, B.S., S.L., K.H.F., J.V.M., N.A., P.K., M.T.W., G.S.C., S.M.T., C.V., G.L.C., P.C., M.J.L.C., S.G., R.A.F.G., N.M., G.R.O., A.S.P.R., U.R., V.V., and A.W. analyzed data; and S.P.S.G., T.J.B., and J.V.M. wrote the paper.

The authors declare no conflict of interest.

This article is a PNAS Direct Submission.

Published under the PNAS license.

Data deposition: All data are deposited with the International Ocean Discovery Program, [iodp.pangea.de](http://iodp.pangea.de) (Expedition 364).

<sup>1</sup>To whom correspondence may be addressed. Email: [sean@ig.utexas.edu](mailto:sean@ig.utexas.edu).

<sup>2</sup>A complete list of the Expedition 364 Scientists can be found in *SI Appendix*.

This article contains supporting information online at [www.pnas.org/lookup/suppl/doi:10.1073/pnas.1909479116/-DCSupplemental](http://www.pnas.org/lookup/suppl/doi:10.1073/pnas.1909479116/-DCSupplemental).

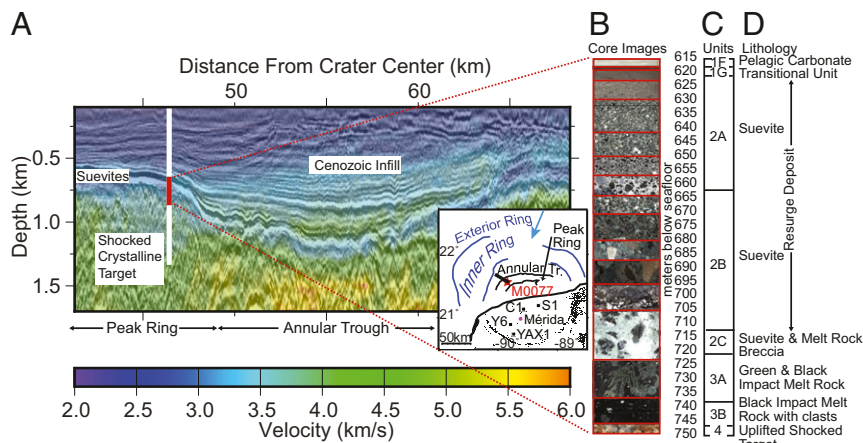


**Fig. 1.** (A) Seismic reflection image shown in depth with full waveform velocities overlain; line runs from southeast to northwest, including the location of Site M0077, and radially outward across the annular trough. The suevite interval within M0077, the focus of this paper, is shown in red, which maps to a low-velocity zone beneath the crater floor. The map in *Inset* shows the location of crater rings, drill sites (in the text), the seismic image, and the direction that ocean waters reentered the crater after formation. Expansion shows (B) representative core images in stratigraphic order with depths, (C) lithologic units, and (D) lithology.

(13) or to melt–water interaction (MWI) similar to molten fuel coolant interaction (MFCI) in volcanic processes (16, 22–24).

The K-Pg impact event resulted in a globally distributed ejecta layer, which at distal sites (>6,000 km from Chicxulub), is highly condensed (2- to 3-mm thick) and contains altered microkrystites and shocked minerals (25). These impact deposits, which formally were deposited within the Cenozoic (Danian) (26), thicken and become more stratigraphically complex with proximity to the crater (25). K-Pg boundary sections around coastal and shelf sites in the Gulf of Mexico and Caribbean show a mixture of material delivered by airfall, shelf collapse, debris flows, and tsunami (27–32). Within the deep water Gulf of Mexico, earthquake energy from the impact triggered gravity flows on continental slopes, generating the largest known event deposit on Earth (33). Within the Chicxulub impact structure, the boundary event deposit was drilled onshore within the annular trough (sites ICDP Yaxcopoil-1 and Yucatan-6) and the central basin (sites Sacapuc-1 and Chicxulub-1) (Fig. 1) (11, 34–36).

These records of the K-Pg boundary offer critical insights into the environmental effects of the Chicxulub impact and connections to the global extinction event (25, 37). The sedimentary target rocks, composed of volatile-rich marine carbonates and evaporites, have been a key focus of studies considering possible extinction mechanisms (38–43). Yaxcopoil-1 penetrated an intact Cretaceous Albian to Campanian slump block that consisted of 27% anhydrite and >70% carbonates (44, 45). Studies of the deposits outside the crater suggest that the deeper sedimentary target may have been even more evaporite rich (49 to 60% anhydrite) (46, 47). In the atmosphere, sulfate combines with water vapor to form sulfate aerosols that impede solar insolation; models of global climate response to a conservative 100 Gt of sulfur released by the Chicxulub impact into the K-Pg atmosphere indicated that global surface temperatures would have declined by >20 °C and that disruption of the Earth's climate could have lasted ~30 y (48). This scenario is consistent with proxy data indicating sea surface cooling in the months to years after the impact (30).

A sudden release of  $425 \pm 60$  Gt of  $\text{CO}_2$  and  $325 \pm 60$  Gt of S was recently calculated by Artemieva et al. (49) using new constraints for the impact angle and direction of the Chicxulub impactor from Collins et al. (50); these larger sulfate amounts might result in prolonged cooling. Furthermore, Mössbauer analyses of boundary clay from proximal and distal sites have revealed that Fe nanoparticles, formed during the impact, served as nuclei for

aerosols, causing prolonged darkness (51, 52). Ejecta descending from high altitudes can radiate heat and potentially ignite wildfires (53–57). Soot within the K-Pg boundary layer indicates that extensive impact-induced fires occurred instantaneously or within months of the impact (58) and could have intensified global cooling (59). One of the major objectives of drilling at the peak ring was to explore evidence for the drivers of these profound environmental changes that were potentially responsible for the severity of the mass extinction at the K-Pg boundary.

IODP-ICDP Expedition 364 drilled into the offshore portion of the Chicxulub impact crater (2, 3). Site M0077 (Fig. 1) was located high on the topographic peak ring, providing a unique setting for examining the K-Pg boundary within the crater; the site was selected based on seismic images that suggested that the K-Pg boundary was located in a valley within the peak ring, which itself is elevated ~400 m above the crater floor. We proposed that this location would preserve the full sequence of impact-related rocks and transition into the earliest Paleogene without significant erosion from postimpact slumping induced by earthquake aftershocks (Fig. 1). Site M0077 recovered core from 505.70 to 1,334.73 m below seafloor (mbsf) at nearly 100% recovery (2, 3).

### Observations of the K-Pg Boundary Sedimentary Sequence

The recovered core at Site M0077 is broadly subdivided into 4 units (Fig. 1) (60). Unit 1 is 111.63-m-thick postimpact sedimentary rock. Unit 2 is 104.28-m thick and dominantly suevite. Unit 3 is 25.41-m-thick impact melt rock with some clasts present. Unit 4 consists of shocked granitic target rocks, preimpact sheet intrusions, and intercalations of suevite and impact melt rock. Here, we examine the sedimentology and geochemistry of Unit 1G, referred to as the Transitional Unit (61), and Units 2 and 3, which constitute the upper peak ring impactites cored from 617.34 to 747.14 mbsf. Here, we provide core descriptions, 0.3-mm-resolution X-ray computed tomography (CT) imaging of clasts, matrix and structure, paleomagnetic data, visual line logging of clasts within the cores  $\geq 0.5$  cm in size, and machine learning identification and analysis of clast size, shape, and sorting for the ~130-m-thick K-Pg boundary deposit. Smear slide observations and organic geochemical analyses were made of samples in the uppermost ~3 m of the section of Unit 2A and Unit 1G.

Photos of the split cores of Unit 3 (Fig. 1B) illuminate an upward transition from impact melt rock (Unit 3) to breccia





largely consisting of black impact melt rock fragments within a green and gray matrix (Unit 2C). The upper portions of Unit 3 and lower parts of Unit 2 also include large target rock clasts. Thus, we describe this section as including impact melt rock, impact melt rock breccia, and suevite (Fig. 1B). Within Unit 2, the overall clast size decreases upcore.

Geological line logging applied on Unit 2 (the suevite interval) was used to catalog all clasts larger than 5 mm along a transect of the cores from 672.01 to 715.93 mbsf (Fig. 3 and *Methods*). Analyzed parameters included clasts/meter, clast size, matrix- vs. clast-supported grains, roundness, sorting, and a broad categorization of lithology. From 706.00 to 715.93 mbsf, clasts per meter were low (<50), clast sizes were up to 10 cm, roundness increased from angular to subangular, and the section was poorly sorted (Fig. 3). Lithologically, the abundance of clasts in this lower section was >60% impact melt rock, ~20% sedimentary target rocks (carbonate, siltstone, and chert), and ~10% crystalline target rocks. In contrast, from 698.00 to 706.00 mbsf clasts per meter increased by ~50%, clast size decreased, and roundness and sorting increased upcore (Fig. 3). The proportion of melt rock fragments increased by ~10% in this interval at the expense of carbonate target rock clasts. From 672.01 to 698.00 mbsf, the number of clasts per meter and sorting increased, and clast size decreased upsection. The abundance of crystalline target rock clasts in the clast population decreased to <5% in this interval, and the abundance of sedimentary target clasts increased. None of the 2,793 clasts examined by the geological line logging method were identified as evaporites (anhydrite, gypsum, or halite).

Lithology and geochemistry of Unit 2, both matrix and clasts, were also examined using 50 2-cm-long samples (60). Each sample was classified by its mineral mode and chemical composition using bulk powder X-ray diffraction (XRD) analysis and X-ray fluorescence (XRF). The total percentages of gypsum and anhydrite recorded by XRD were 0.73 and 0.04%, respectively. Furthermore, no anhydrite or gypsum minerals were observed in petrographic examination of 85 thin sections, and less than 0.7 wt % S was determined in micro-X-ray fluorescence ( $\mu$ XRF) scans of 53 thin sections and LECO CS-300 carbon-sulfur analyses (*Methods* and *SI Appendix*, Figs. S1 and S2) (60). There are 3 outliers, 2 of which (Core 40R-1: 0.63 wt % S and Core 40R-2: 0.44 wt % S) are identified as pyrite ( $\text{FeS}_2$ ) grains by  $\mu$ XRF and petrographic observation (*SI Appendix*, Fig. S3). The third outlier detected by carbon-sulfur analysis (Core 74R-1: 0.43 wt % S) is

also likely pyrite. Lastly, detailed petrographic analyses of 12 suevite samples were performed using electron beam methods, and no anhydrite or gypsum was observed (*Methods*). In summary, our multimethod analysis determined that the suevite sequence in the IODP-ICDP 364 core was almost entirely devoid of gypsum and anhydrite, and sulfur-bearing phases were limited to pyrite, chalcopyrite, and minor accessory minerals (3).

In addition to line logging, a machine learning routine was developed to analyze clast characteristics using high-resolution core photographs (Fig. 3 and *Methods*). A convolutional neural network extracted features based on textural patterns, and then, clasts were classified using a segmentation routine (*SI Appendix*, Fig. S4). Clast size, roundness and sorting, area per meter, and clast vs. matrix support were determined from the data. These values are compared with the line logging analyses of the same characteristics on the transect of clasts (Fig. 3). Both methods showed that (i) the numbers of clasts and clast size were inversely correlated; (ii) within the analyzed breccia, a shift from clast to matrix supported occurred between 708 and 706 mbsf; (iii) the interval from 698 to 706 mbsf represented a transition in roundness, sorting, and clast size; and (iv) above ~690 mbsf, numbers of clasts, matrix support, and sorting increased, while clast sizes decreased.

X-ray CT images of the 3-dimensional scans of the Site M0077 cores yielded information on the relative CT numbers (a proxy for density) of the matrix and clasts throughout the suevite (*SI Appendix*, Fig. S5). Key CT observations are as follows. (i) The black impact melt rocks (Fig. 1) in Unit 3B included partially digested clasts (*SI Appendix*, Fig. S5). (ii) Clasts of the black impact melt rock in Unit 3A were observed in a matrix of the green impact melt rock (Fig. 1). (iii) In Unit 2C, the matrix transitioned from a higher CT number (light gray in *SI Appendix*, Fig. S5) characteristic of melt rock in Unit 3 to a lower CT number (darker gray in *SI Appendix*, Fig. S5) identified with the electron microprobe as a calcite, silica, and zeolite groundmass observed throughout the suevite in Units 2A and 2B. (iv) From 698 to 706 mbsf in Unit 2B, the matrix was relatively uniform, and the interval included the shallowest multicentimeter clasts. (v) In Units 2A and 2B above 698 mbsf, fining upward clast sizes dominated. (vi) In Unit 2A, local reverse grading was observed, and from 617.5 to 625 mbsf, some layering is present (Fig. 4 C, H, and I). (vii) the interval from 617.34 to 617.44 mbsf in Unit 2A was a 10-cm-thick unidirectional cross-bedded deposit (Fig. 4 F and G).

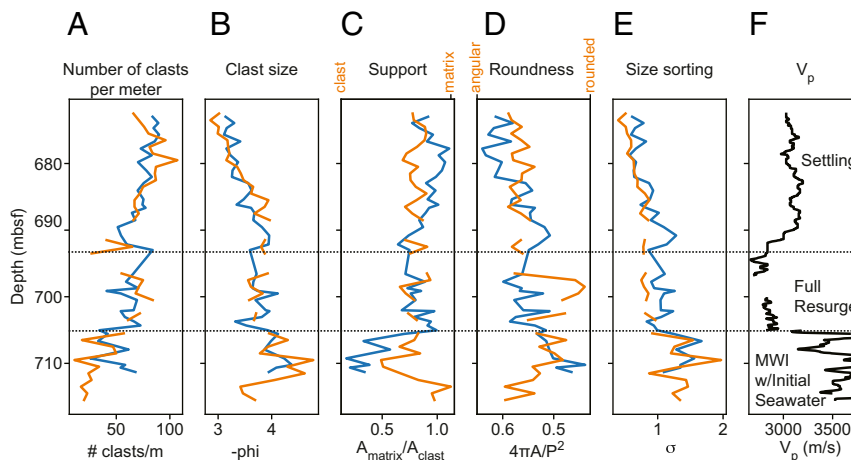


**Fig. 3.** Combined analysis of the larger-clast size portion of the suevite using line-scan images of the Hole M0077A split cores; A to E show data from visual line logging in orange and machine learning analysis in blue. F shows downhole sonic log from Site M0077 over the same interval. Interpreted intervals are shown for MWI deposits, resurge of ocean waters cresting peak ring at Site M0077, and start of settling in the now-flooded crater to generate the resurge deposit.

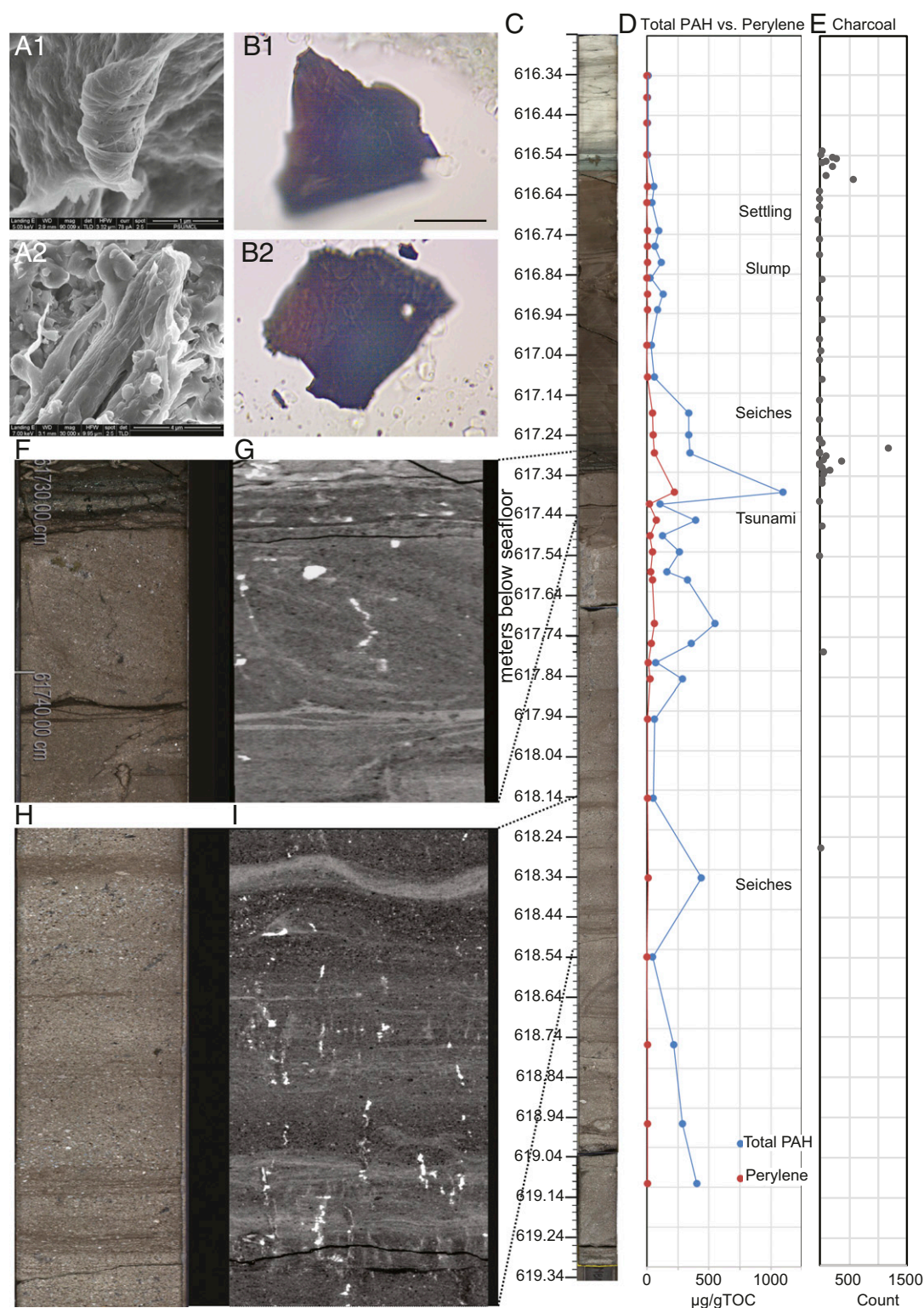


**Fig. 4.** Core 40 from Site M0077 data. (A1 and A2) Scanning electron microscope images of charcoal fragments. (B1 and B2) Reflected light microscope images of charcoal fragments at 1,600 $\times$  magnification. (C) Line-scan image of Core 40 showing the Transition Layer (Unit 1G) and the uppermost suevite (Unit 2A). (D) Total PAH data and the dominant PAH observed in the cross-bedded layer, perylene, both shown as micrograms per gram of total organic carbon (TOC). (E) Charcoal counts showing concentrations just above the interpreted tsunami and near the top of Unit 1G. (F) Zoomed-in view of line-scan image of the cross-bedded interval at the top of Unit 2A interpreted as being deposited by a tsunami. (G) Unwrapped CT scan of same portion of core as F. (H) Line-scan image of higher-energy deposits beneath the tsunami interpreted as seiches. (I) Unwrapped CT scan of same portion of core as H.





tsunami, formed by the outward uplift of the transient crater rim and the subsequent deposition of proximal ejecta into the shallow seas surrounding the crater (figure 5 in ref. 71), would propagate outward in all directions across the Gulf, where central Mexico was the closest shallow water region and shoreline. The subsequent return flow of water, the “resurge” into the crater, is expected to be dominated by ingress from the north–northeast rim gap. After large-volume resurge waves enter the impact basin, phreatomagmatic-style events (MWI) will gradually switch off and substantially reduce temperatures at the seafloor (Fig. 2E). Simplified 1-dimensional “dam break” modeling of the flooding of the crater up to the depth of the peak ring (*Methods* and *SI Appendix, Fig. S9*) suggests that the timing of full resurge is 30 to 60 min postimpact for a water depth at the crater rim exceeding 1 km. Complete flooding of the crater likely took considerably longer. We interpret the increase in rounding and sorting in Unit 2B from 698 to 706 mbsf to signify the return of ocean water (Figs. 2E and 3) and the fining upward deposit from 617 to 698 mbsf (Fig. 3) to represent the bulk of the resurge deposit, which occurred in a progressively flooding crater (Fig. 2F).

Evidence for the arrival of the resurge to the peak ring being recorded in the deposit from 698 to 706 mbsf includes (i) the presence of the shallowest multicentimeter clasts at ~698 mbsf; (ii) that this layer is reduced in sonic velocities, suggesting a higher porosity, more rapidly deposited section; and (iii) a relatively continuous reduction in grain size and increase in sorting upcore above 698 mbsf (Fig. 3). Size sorting of large clasts near the base of Unit 2B, due to the presence of water, could be the cause for the observed low-frequency reflector present below the low-velocity zone that marks the suevite interval in seismic data (Fig. 1A) (4). The observation of both positive and negative paleomagnetic inclinations within samples from Unit 2B (*SI Appendix, Fig. S7*) suggests that this unit was deposited at lower temperatures than Unit 2C as would be expected in a now flooded crater. A combination of entrained clasts retaining their predepositional magnetization and new magnetization produced by the creation of secondary magnetic minerals in a long-lived, postimpact hydrothermal system (3) are likely responsible for the observed variations in remnant magnetism.

The flooded crater likely continued to be a high-energy environment due to large magnitude earthquake aftershocks and gravity flow processes from the collapsed central uplift and the rapidly formed inner rim (33, 34). We interpret the erosional contact at 642.57 mbsf at the base of Unit 2A as resulting from a gravity flow and the presence of 25 graded beds within Unit 2A (Fig. 4I) as evidence of seiches within the crater possibly triggered by earthquake energy and slumping. Chicxulub created Mw10–11 earthquakes (33), and the seismic shaking has been shown to generate seiches ~2,000 km away in local basins (72). However, the bulk of Unit 2A continues to show fining upward clast sizes and increasing sorting reflective of a settling process in a flooded crater with these punctuated higher-energy events (Fig. 2F).

The top of the suevites of Unit 2A (617.34 mbsf) is marked by a <10-cm-thick cross-bedded interval. These structures exhibit a unidirectional flow path of sand- to fine gravel-sized particles (Fig. 4 F and G). The presence of low concentration of PAHs below the cross-bedded unit is interpreted to be generated by either combusted marine biomass or reworked Cretaceous or older hydrocarbons in the target rocks. However, the increase in concentration of PAHs, particularly the terrestrial compound perylene, that is observed to peak in the cross-bedded layer (Fig. 4) requires that a source of terrestrial material entered the crater during deposition of the uppermost Unit 2A (Fig. 4D). The abundant reworked Maastrichtian planktic foraminifera at the top of Unit 2A indicate redeposition of sediments that were unconsolidated at the time of the impact. We, therefore, suggest that the uppermost 10-cm, cross-bedded suevite represents the

return of the outward-directed rim-wave tsunami reflected back from Gulf of Mexico coastlines, which carried terrestrial signatures and suspended unconsolidated marine sediments (illustrated in Fig. 2G). The transport path was potentially across the shelf separating the Mexican highlands ~800 km to the west–southwest from the newly formed crater. Based on modeling, the arrival time of the rim-wave tsunami trains on the far side of the Gulf of Mexico was 2 to 3 h after the impact (33), and reflections across the shelfal depths from the west are also likely hours in duration. Thus, we suggest that this tsunami energy was reflected back into the impact basin within the first day of the Cenozoic and that these tsunami waters were turbid and capable of transporting soil biomarkers.

Deposition of Unit 1G likely took place in less than a few years after the impact (61). We interpret the normal graded couplets within the lower part of this unit to represent a significant reduction in wave energy compared with Unit 2A, as sedimentary features, such as cross-bedding, are rare and grain size is considerably reduced (Fig. 4C). The decrease in grain size and lower-energy couplets in Unit 1G imply that lower-magnitude aftershocks and/or gravity flows occurred in the impact basin over longer timescales than the seiches observed in Unit 2A.

**Evidence for Fire.** High abundances of charcoal are present in Unit 1G 4 cm above the top of the presumed tsunami deposit (Fig. 4) and also within a few centimeters of the top of Unit 1G. The relationship of the lower layer with the high-energy deposit suggests that these particles were either transported into the crater by reflected tsunami but settled more slowly than the remainder of the material due to density differences as energy subsided or are derived via airfall. Charcoal likely originated from impact-related combustion of forested landscapes surrounding the Gulf of Mexico, as the impact site was entirely marine. The shallower charcoal layer (Fig. 4E) may reflect airfall with mixing into the overlying Unit 1F by bioturbation or reworking. Wildfires can be spawned in 2 ways by a large impact: directly by the impact plume or by reentering ejecta (56, 73, 74). For Chicxulub, the plume is considered to emit sufficient thermal radiation to ignite flora up to 1,000 to 1,500 km from the impact site (73). High-velocity ejecta reentering the Earth’s atmosphere emits thermal radiation that is sufficient to ignite dry plant matter and char living flora at sites within a few thousand kilometers from the crater and may directly ignite living flora at more distal locations, where the thermal pulse is delivered to the Earth’s surface over a longer time period (74). Strong atmospheric disturbances associated with the impact could have extinguished some of these fires and emplaced unburnt, partially burnt, or fully burnt plant materials within the atmosphere (58, 73). Thus, the lower charcoal layer observed at Site M0077 could stem from charred proximal flora from the central Mexican shorelines ~800 km away ignited by the impact plume and delivered back to the crater by tsunami or other mechanisms. The shallow water depths to the south and southwest of Chicxulub mean that the rim-wave tsunami could have reflected from the central Mexican highlands and reached Chicxulub within hours of the impact without transiting deep water. The upper layers of charcoal were delivered to the crater years after the event (near top of Unit 1G) (61), probably from atmospheric rainout of fire-generated particles from wildfires around the globe.

### Broader Implications

In summary, the Expedition 364 core of the Chicxulub peak ring contains the most complete and expanded record of the immediate aftermath of the K–Pg mass extinction to date. Generation of a deep crater, with a large opening in the rim that allowed rapid flooding of the crater by seawater, produced accumulation rates among the highest known in the geologic record (130 m/d). Preservation of these extreme sediment accumulation rates within the

impact basin allows us to resolve the geological processes that occurred over minutes to years after the impact event. In particular, the recovered sedimentary section lacks evaporites, supporting impact-generated sulfate aerosol production and extinction mechanisms, including global cooling and limitations on photosynthesis. The presence of melt breccia and suevite in cores suggests potential MWIs, and rounding and sorting provide evidence for ocean resurge. Finally, graded beds, a cross-bedded layer with terrestrial signatures, and charcoal provide evidence for seiches within the crater, a reflected tsunami, and some proximal fire generation within the first day of the Cenozoic.

## Methods

Forty-one thin sections of the suevite interval between core sections 40–2 and 87–2 were examined for the presence of gypsum ( $\text{CaSO}_4 \cdot 2\text{H}_2\text{O}$ ), anhydrite ( $\text{CaSO}_4$ ), and halite ( $\text{NaCl}$ ) under a transmitted light microscope. Clasts identified as possible halite or sulfate phases are analyzed by small trace elemental maps on a Bruker M4 Tornado  $\mu\text{XRF}$  scanner following the methodology of de Winter and Claeys (75). Thin sections from Unit 1G were examined microscopically under plane and cross-polarized light using standard petrographic techniques. Bedding, lamination, ichnofabric, and other sedimentary structures were identified. Grains, matrix material, and diagenetic products were classified; their mineralogy was evaluated; and maximum grain size was measured using the microscope's reticle.

High-resolution, semiquantitative major and trace elemental maps of 53 polished thick sections between core sections 40–2 and 96–2 were produced by using the Bruker M4 Tornado  $\mu\text{XRF}$  scanner available at the Vrije Universiteit Brussel (75) (*SI Appendix, Fig. S1*). The elemental mapping measurements were executed using an Rh source and 2 XFlash 430 Silicon Drift detectors under vacuum conditions (20 mbar), with short acquisition times per spot size (1 ms per spot with a size of 25  $\mu\text{m}$ ) and maximized source energy settings (600  $\mu\text{A}$ , 50 kV). Bulk compositions of the thick sections were quantified by identifying the X-ray peaks in a representative boundary spectrum within the high-resolution color map. Major elements were expressed as oxides ( $\text{Na}_2\text{O}$ ,  $\text{MgO}$ ,  $\text{Al}_2\text{O}_3$ ,  $\text{SiO}_2$ ,  $\text{K}_2\text{O}$ ,  $\text{CaO}$ ,  $\text{TiO}_2$ ,  $\text{MnO}$ ,  $\text{Fe}_2\text{O}_3$ ), whereas trace elements are in elemental configuration, as these are present at much lower concentration levels (P, S, Cl, V, Cr, Ni, Cu, Zn, Rb, Sr, Zr, Ba). The limit of quantification of elemental sulfur in the M4 Bruker Tornado  $\mu\text{XRF}$  is conservatively estimated to be 0.1 wt % (*SI Appendix, Fig. S2*). This limit is based on the quantification of  $\mu\text{XRF}$  maps of pellets prepared from carbonate reference materials NIST SRM 1d (National Institute of Standards & Technology) and BCS CRM 513 (Bureau of Analyzed Samples Ltd.). The limit of detection of S with this technique is 0.033 wt %.

Back-scattered electron imaging, energy-dispersive spectrometry, and X-ray intensity mapping were used to describe the petrography of 12 suevite samples from the upper peak ring section between 620 and 708 mbsf. This work was done with a JEOL-JXA 8530F electron microprobe at Arizona State University's Eyring Materials Center. For imaging and EDS analyses, an accelerating voltage of 15 kV, a beam current of 15 nA, and a focused beam were used. The X-ray intensity maps used an accelerating voltage of 20 kV, a beam current of 60 nA, a dwell time of 20 ms, and a beam diameter of 20  $\mu\text{m}$ . These supplemental studies confirmed the absence of anhydrite or gypsum in the studied suevite.

The Chicxulub cores were scanned using a Toshiba Aquilion Prime Dual Energy Helical CT scanner at Weatherford Laboratories in Houston. This produces a series of axial cross-section maps of attenuation coefficients at 2 energy levels (135 and 85 kV). Each cross-section represents 0.3 mm of core depth and has a spatial resolution of 0.25 mm. Processing of the raw CT was performed by Enthougt Inc. (76). CT depth values (meters core composite depth below sea floor) are artificially lengthened relative to drillers depth (called meters below seafloor) due to overlaps in cores not being accommodated. CT images map the attenuation of X-rays at a given location in the core; this is represented using grayscale images, where darker grays are low attenuation and light gray is high attenuation (Fig. 4 E and F and *SI Appendix, Fig. S5*). X-ray attenuation is correlated to both the bulk density and average atomic number of a sample region. Dual-energy CT scans provide a mechanism to separate these effects (77).

Line logging of drill cores is useful in the analysis of relative changes through the infill of impact craters, including slump and resurge deposits due to a marine target environment. This technique has been successfully applied to the Lockne, Tvären, and Chesapeake Bay impact structures (18–19, 78). In this method, every clast with a length axis larger than a certain cutoff size (here, 5 mm) that touches a line drawn along the core is assessed for size, roundness, and lithology (Fig. 3). Instead of using actual drill core, this

technique was applied to high-resolution core photos with the use of the image analysis software jMicrovision (version 1.2.7). In the suevite (M0077 Unit 2), 2,376 clasts were analyzed between depths 672.01 and 715.93 mbsf, and an evaluation of the nature of their groundmass, whether matrix or clast supported, was done (i.e., if clasts were in contact or not with adjacent clasts). Roundness was estimated with the use of grain shape comparator (i.e., a standard diagram with drawings of grain shapes). Here, a diagram with only 4 shapes (i.e., angular, subangular, subrounded, rounded) was decided to be the most convenient (cf. ref. 79). CT images aided the lithological determinations. The lithologies were (preliminarily) classified into 17 categories that include (i) melt rocks of different colors and textures; (ii) upper target (sedimentary rock, mainly carbonates); and (iii) lower target (crystalline rock and quartzite). The granulometric data were treated statistically as variations per meter, which allowed plots of clast frequency per meter and size sorting. Owing to the large amount of data, clast vs. matrix support was plotted as a ratio per meter. Uncertainty in clast size is largest for the smallest analyzed clasts. We estimate that, at 15 pixels per 1 mm, a 5-mm grain could have an 8% error in the clast size value but that this uncertainty reduces greatly with increasing clast size.

In order to efficiently examine a larger number of clasts, a deep learning model was applied to the high-resolution core photographs (Fig. 3). The pipeline has 2 stages: classification (*SI Appendix, Fig. S4*) and segmentation/shape analysis. In the classification step, a machine learning model is used to assign a lithology label to every pixel in the core photographs. The digital core photographs are red–green–blue images and have 3 features directly associated with each pixel location—the amount of red, green, and blue light that makes up the color of the pixel. This is local information, and classifying a pixel based only on color features neglects the spatial and textural context of a pixel. The images are passed to a pretrained convolutional neural network (VGG-16) (80), and intermediate activations are extracted, forming a hypercolumn of spatial convolutions that provide textural features useful for classification (81). Training data are created by manually labeling representative pixels that belong to each of the lithology types represented in the core images. The labeled pixels along with their associated hypercolumns are used to train a machine learning model (XGBoost) (82) to predict a lithology label for every pixel in the core images. The initial classification results are spatially regulated using a fully connected conditional random field (83). Individual clasts are observed in the classified images by identifying contiguous regions of pixels with the same lithology label that exceed a size threshold. Each clast is analyzed in terms of shape (perimeter, area), position, orientation, and aspect ratio using the image analysis package scikit-image (84). The circularity of each clast ( $4 \times \pi \times \text{area} / \text{perimeter}$ ) is used as a roundness metric. The ratio of clast area to matrix area was calculated as a proxy for clast/matrix support.

Sedimentologic analyses include visual observation of the split cores and point counting. Point counting to determine clast–matrix percentages was completed using jMicrovision on line-scan images. Each value represents 300 points counted on each core piece (*SI Appendix, Fig. S6*).

During the Expedition 364 Onshore Science Party, 83 nonazimuthally oriented paleomagnetic cylinders were obtained from Units 2 and 3 (*SI Appendix, Fig. S7*). These samples were stepwise demagnetized using alternating field demagnetization up to at least 85 mT and measured using 2G Enterprises superconducting magnetometers at Rutgers University or CEREGE (France) or an AGICO JR-5 spinner magnetometer at CEREGE. Characteristic magnetization directions were obtained for the highest coercivity, origin-trending magnetization component within each sample using principal component analysis (85). Ferromagnetic mineralogy and Curie temperatures were determined via high-temperature magnetic susceptibility measurements using an AGICO Kappabridge susceptibility meter at CEREGE.

Charcoal was first identified in smear slides using a Zeiss Axioskop microscope under bright-field light at 1,600 $\times$  magnification. This illumination allowed the characteristic wood structure to be observed. The distribution and character of charcoal in samples were determined in thin sections using Zeiss Axioimager petrographic microscopes using bright-field illumination. Grains were also observed in an FEI Nova NanoSEM 630 FE scanning electron microscope. The relative abundance of charcoal was determined from the area of grains in 25 fields of view at 1,600 $\times$  magnification using the NIH's ImageJ software (*SI Appendix, Fig. S8*).

The flooding rate of the Chicxulub crater at the approximate location of the Expedition 364 drill site on the peak ring was estimated assuming that resurge was dominated by ingress of water from the deep preimpact basin to the north–northeast (*SI Appendix, Fig. S9*). Analytical solutions to the 1-dimensional dam break problem (86) for 3 different dam heights ( $h_0 = 0.5, 1, \text{ and } 2 \text{ km}$ ) were found assuming that water entered the crater on one side through a deep channel in the rim, flowed across the crater, and



reflected off the inside of the crater rim on the opposite (south–southwest) side of the crater. The different dam heights represent alternative estimates of the depth of water at the onset of the resurge. The upper estimate (2 km) represents the estimated maximum depth of the preimpact basin at the edge of the crater and is consistent with the numerical impact simulation shown in figure 5 of the work by Collins et al. (71). Flooding of the crater up to the depth of the peak ring (500 m above the crater floor) is expected to take 30 min to 1 h (*SI Appendix, Fig. S9*). The approximation neglects various factors that might delay the resurge, such as drag between the water and the crater floor and interactions between the flood water and the hot melt sheet, which might vaporize some of the water and generate MWI products.

In order to analyze the cores for biomarkers (Fig. 4D and *SI Appendix, Fig. S10*), core samples (~20 g) were surface cleaned by sonication in ultrapure water 2 times for 15 min to remove any drilling fluid. After, the samples were freeze dried and 3 times sonicated for 15 min in dichloromethane and methanol (9:1 vol/vol). After drying, the samples were ground using a pestle and mortar and Soxhlet extracted for 72 h using a mixture of dichloromethane and methanol (9:1 vol/vol). The extracts were passed through a Pasteur pipette containing activated copper powder to remove the elemental sulfur. Excess solvent was carefully removed under nitrogen. The weighed extracts were then fractionated by small-scale column liquid chromatography. The sample (up to 10 mg) was applied to the top of a small column (5 × 0.5-cm interior diameter) of activated silica gel (150 °C, 8 h). The saturated hydrocarbon fraction was eluted with *n*-hexane (4 mL), the aromatic hydrocarbon fraction was eluted with *n*-hexane and dichloromethane (4 mL, 9:1 vol/vol), and the polar fraction was eluted with a mixture of dichloromethane and methanol (4 mL, 1:1 vol/vol). The saturated and aromatic hydrocarbon fractions were analyzed by gas chromatography (GC)–mass spectrometry (MS). GC–MS analysis was performed using an Agilent 5975B MSD interfaced to an Agilent 6890 gas chromatograph, which was fitted with a DB-5MS UI capillary column (J and W Scientific; 60 m, 0.25-mm inner diameter, 0.25-μm phase thickness). The GC oven was ramped from

40 °C to 325 °C at a heating rate of 3 °C/min, with initial and final hold times of 1 and 30 min, respectively. Samples were dissolved in *n*-hexane and injected on column using an Agilent 7683B autosampler. Helium (constant flow 27 cm/s) was used as the carrier gas. The MS was operating with ionization energy of 70 eV, a source temperature of 230 °C, and an electron multiplier voltage of 1,706 V, scanning a mass range of 50 to 550 amu. Aromatic hydrocarbon compounds were identified by comparison of mass spectra and by matching retention times with those of reference compounds reported previously (87). The unsubstituted PAHs, including benzo(a)pyrene and perylene (the ratio of these 2 PAHs is shown in *SI Appendix, Fig. S10*), have a molecular ion of *m/z* 252. They were identified by comparing their retention times with those of reference compounds.

**ACKNOWLEDGMENTS.** We thank the captain and crew, drilling team, and technical staff who participated in shipboard and/or shore-based operations. We thank the editor and 2 anonymous reviewers. W. Zylberman and J. Gattacceca are thanked for assistance with paleomagnetic measurements. Data and samples can be requested from IODP. The European Consortium for Ocean Research Drilling (ECORD) implemented Expedition 364 with funding from the IODP and the ICDP. US participants were supported by the US Science Support Program and National Science Foundation Grants OCE 1737351, OCE 1736826, OCE 1737087, OCE 1737037, OCE 1736951, and OCE 1737199. J.O. was partially supported by Grants ESP2015-65712-C5-1-R and ESP2017-87676-C5-1-R from the Spanish Ministry of Economy and Competitiveness and Fondo Europeo de Desarrollo Regional. B.S. thanks Curtin University for an Australian Postgraduate Award. J.V.M. was funded by Natural Environment Research Council Grant NE/P005217/1. K. Grice thanks Australia Research Council for Grant DP180100982 and Australia New Zealand IODP Consortium for funding. The Vrije Universiteit Brussel group is supported by Research Foundation Flanders (FWO) and BELSPO; P.K. is an FWO PhD fellow. This is University of Texas Institute for Geophysics Contribution 3634.

- H. J. Melosh, *Impact Cratering: A Geologic Process* (Oxford Monographs on Geology and Geophysics, Oxford University Press, Oxford, 1989), vol. 11, p. 253.
- J. V. Morgan et al., The formation of peak rings in large impact craters. *Science* **354**, 878–882 (2016).
- J. Morgan, S. Gulick, C. L. Mellett, S. L. Green; The Expedition 364 Scientists, “Chicxulub: Drilling the K-Pg impact crater” in *Proceedings of the International Ocean Discovery Program* (International Ocean Discovery Program, 2017), vol. 364.
- G. L. Christeson et al., Extraordinary rocks from the peak ring of the Chicxulub impact crater: P-wave velocity, density, and porosity measurements from IODP/ICDP Expedition 364. *Earth Planet. Sci. Lett.* **495**, 1–11 (2018).
- G. S. Collins, H. J. Melosh, J. V. Morgan, M. R. Warner, Hydrocode simulations of Chicxulub crater collapse and peak-ring formation. *Icarus* **157**, 24–33 (2002).
- U. Riller et al.; IODP–ICDP Expedition 364 Science Party, Rock fluidization during peak-ring formation of large impact structures. *Nature* **562**, 511–518 (2018).
- P. J. Barton et al., “Seismic images of Chicxulub impact melt sheet and comparison with the Sudbury structure” in *Large Meteorite Impacts and Planetary Evolution IV*, U. W. Reimold, R. L. Gibson, Eds. (Geological Society of America Special Paper 465, Denver, CO, 2010), pp. 103–113.
- J. V. Morgan et al., Full waveform tomographic images of the peak ring at the Chicxulub impact crater. *J. Geophys. Res. Solid Earth* **116**, B06303 (2011).
- S. P. S. Gulick et al., Geophysical characterization of the Chicxulub impact crater. *Rev. Geophys.* **51**, 31–52 (2013).
- E. M. Shoemaker, E. C. Chao, New evidence for the impact origin of the Ries Basin, Bavaria, Germany. *J. Geophys. Res.* **66**, 3371–3378 (1961).
- P. Claeys, S. Heuschkel, E. Lounejeva-Baturina, G. Sanchez-Rubio, D. Stöffler, The suevite of drill hole Yucatán 6 in the Chicxulub impact crater. *Meteorit. Planet. Sci.* **38**, 1299–1317 (2003).
- D. Stöffler, R. Grieve, “Impactites” in *Metamorphic Rocks: A Classification and Glossary of Terms, Recommendations of the International Union of Geological Sciences*, D. Fettes, J. Desmons, Eds. (Cambridge University Press, Cambridge, UK, 2007), pp. 82–125.
- G. R. Osinski, R. A. Grieve, J. G. Spray, The nature of the groundmass of surficial suevite from the Ries impact structure, Germany, and constraints on its origin. *Meteorit. Planet. Sci.* **39**, 1655–1683 (2004).
- C. Meyer, M. Jébrak, D. Stöffler, U. Riller, Lateral transport of suevite inferred from 3D shape-fabric analysis: Evidence from the Ries impact crater, Germany. *Geol. Soc. Am. Bull.* **123**, 2312–2319 (2011).
- D. A. Kring, Hypervelocity collisions into continental crust composed of sediments and an underlying crystalline basement: Comparing the Ries (~24 km) and Chicxulub (~180 km) impact craters. *Geochemistry* **65**, 1–46 (2005).
- N. A. Artemieva, K. Wünnemann, F. Krien, W. U. Reimold, D. Stöffler, Ries crater and suevite revisited—observations and modeling. Part II. Modeling. *Meteorit. Planet. Sci.* **48**, 590–627 (2013).
- D. Stöffler et al., Ries crater and suevite revisited—observations and modeling. Part I. Observations. *Meteorit. Planet. Sci.* **48**, 515–589 (2013).
- J. Örmö, E. Sturkell, M. Lindström, Sedimentological analysis of resurge deposits at the Lockne and Tvären craters: Clues to flow dynamics. *Meteorit. Planet. Sci.* **42**, 1929–1943 (2007).
- J. Örmö, E. Sturkell, J. W. Horton, Jr., D. S. Powars, L. E. Edwards, Comparison of clast frequency and size in the resurge deposits at the Chesapeake Bay impact structure (Eyreville a and Langley cores): Clues to the resurge process. *Spec. Pap. Geol. Soc. Am.* **458**, 617–632 (2009).
- J. W. Horton et al., Origin and emplacement of impactites in the Chesapeake Bay impact structure, Virginia, USA. *Sedimentary Record Meteorite Impacts* **437**, 73–97 (2007).
- G. R. Osinski, R. A. Grieve, A. Chanou, H. M. Sapers, The “suevite” conundrum. Part 1. The Ries suevite and Sudbury Onaping Formation compared. *Meteorit. Planet. Sci.* **51**, 2316–2333 (2016).
- K. Wohletz, G. Heiken, *Volcanology and Geothermal Energy* (University of California Press, Berkeley, CA, 1992), vol. 432.
- R. A. Grieve, D. E. Ames, J. V. Morgan, N. Artemieva, The evolution of the Onaping Formation at the Sudbury impact structure. *Meteorit. Planet. Sci.* **45**, 759–782 (2010).
- A. Wittmann, T. Kenkmann, L. Hecht, D. Stöffler, Reconstruction of the Chicxulub ejecta plume from its deposits in drill core Yaxcopoil-1. *Geol. Soc. Am. Bull.* **119**, 1151–1167 (2007).
- P. Schulte et al., The Chicxulub asteroid impact and mass extinction at the Cretaceous–Paleogene boundary. *Science* **327**, 1214–1218 (2010).
- F. M. Gradstein, *Geologic Time Scale 2012*, J. G. Ogg et al., Eds. (Elsevier, 2012).
- J. Smit, The global stratigraphy of the Cretaceous–tertiary boundary impact ejecta. *Annu. Rev. Earth Planet. Sci.* **27**, 75–113 (1999).
- J. Bourgeois, T. A. Hansen, P. L. Wiberg, E. G. Kauffman, A tsunami deposit at the cretaceous-tertiary boundary in Texas. *Science* **241**, 567–570 (1988).
- P. Schulte et al., Tsunami backwash deposits with Chicxulub impact ejecta and dinosaur remains from the Cretaceous–Palaeogene boundary in the La Popa Basin, Mexico. *Sedimentology* **59**, 737–765 (2012).
- J. Vellekoop et al., Rapid short-term cooling following the Chicxulub impact at the Cretaceous–Paleogene boundary. *Proc. Natl. Acad. Sci. U.S.A.* **111**, 7537–7541 (2014).
- R. A. Denne et al., Massive Cretaceous–Paleogene boundary deposit, deep-water Gulf of Mexico: New evidence for widespread Chicxulub-induced slope failure. *Geology* **41**, 983–986 (2013).
- P. R. Renne et al., Multi-proxy record of the Chicxulub impact at the Cretaceous–Paleogene boundary from Gorgonilla Island, Colombia. *Geology* **46**, 547–550 (2018).
- J. C. Sanford, J. W. Snedden, S. P. Gulick, The Cretaceous–Paleogene boundary deposit in the Gulf of Mexico: Large-scale oceanic basin response to the Chicxulub impact. *J. Geophys. Res. Solid Earth* **121**, 1240–1261 (2016).
- A. R. Hildebrand et al., Chicxulub crater: A possible Cretaceous/tertiary boundary impact crater on the Yucatan Peninsula, Mexico. *Geology* **19**, 867–871 (1991).
- D. A. Kring, W. V. Boynton, Petrogenesis of an augite-bearing melt rock in the Chicxulub structure and its relationship to K/T impact spherules in Haiti. *Nature* **358**, 141–144 (1992).
- J. Urrutia-Fucugauchi, J. Morgan, D. Stöffler, P. Claeys, The Chicxulub scientific drilling project (CSDP). *Meteorit. Planet. Sci.* **39**, 787–790 (2004).
- L. W. Alvarez, W. Alvarez, F. Asaro, H. V. Michel, Extraterrestrial cause for the cretaceous-tertiary extinction. *Science* **208**, 1095–1108 (1980).

38. R. Brett, The Cretaceous-tertiary extinction: A lethal mechanism involving anhydrite target rocks. *Geochim. Cosmochim. Acta* **56**, 3603–3606 (1992).
39. H. Sigurdsson, S. D'Hondt, S. Carey, The impact of the Cretaceous/Tertiary bolide on evaporite terrane and generation of major sulfuric acid aerosol. *Earth Planet. Sci. Lett.* **109**, 543–559 (1992).
40. E. Pierazzo, D. A. Kring, H. J. Melosh, Hydrocode simulation of the Chicxulub impact event and the production of climatically active gases. *J. Geophys. Res. Planets* **103**, 28607–28625 (1998).
41. C. Bell, J. V. Morgan, G. J. Hampson, B. Trudgill, Stratigraphic and sedimentological observations from seismic data across the Chicxulub impact basin. *Meteorit. Planet. Sci.* **39**, 1089–1098 (2004).
42. D. A. Kring, The Chicxulub impact event and its environmental consequences at the Cretaceous-tertiary boundary. *Palaeogeogr. Palaeoclimatol. Palaeoecol.* **255**, 4–21 (2007).
43. S. P. Gulick *et al.*, Importance of pre-impact crustal structure for the asymmetry of the Chicxulub impact crater. *Nat. Geosci.* **1**, 131–135 (2008).
44. T. Kenkmann, A. Wittmann, D. Scherler, Structure and impact indicators of the Cretaceous sequence of the ICDP drill core Yaxcopoil-1, Chicxulub impact crater, Mexico. *Meteorit. Planet. Sci.* **39**, 1069–1088 (2004).
45. J. Belza, S. Goderis, E. Keppens, F. Vanhaecke, P. Claeys, An emplacement mechanism for the mega-block zone within the Chicxulub crater, Yucatán, Mexico based on chemostratigraphy. *Meteorit. Planet. Sci.* **47**, 400–413 (2012).
46. E. L. Ramos, "Geological summary of the Yucatan Peninsula" in *The Gulf of Mexico and the Caribbean*, A. E. M. Nairn, F. G. Stehli, Eds. (Springer, Boston, 1975), pp. 257–282.
47. M. Rebolledo-Vieyra, J. Urrutia-Fucugauchi, Magnetostratigraphy of the Cretaceous/tertiary boundary and early Paleocene sedimentary sequence from the Chicxulub impact crater. *Earth Planets Space* **58**, 1309–1314 (2006).
48. J. Brugger, G. Feulner, S. Petri, Baby, it's cold outside: Climate model simulations of the effects of the asteroid impact at the end of the Cretaceous. *Geophys. Res. Lett.* **44**, 419–427 (2017).
49. N. Artemieva, J. Morgan, Expedition 364 Science Party, Quantifying the release of climate-active gases by large meteorite impacts with a case study of Chicxulub. *Geophys. Res. Lett.* **44**, 10–180 (2017).
50. G. S. Collins *et al.*, Numerical simulations of Chicxulub crater formation by oblique impact. Presented at the 48th Lunar and Planetary Science Conference, The Woodlands, Texas, 20 to 24 March 2017 (Abstract 1832) (2017). <https://www.hou.usra.edu/meetings/lpsc2017/pdf/1832.pdf>. Accessed 9 December 2017.
51. E. Ferrow, V. Vajda, K. Bender-Koch, B. Peucker-Ehrenbrink, P. Willumsen, Multiproxy analysis of a new terrestrial and a marine Cretaceous-Paleogene (K-Pg) boundary site from New Zealand. *Geochim. Cosmochim. Acta* **75**, 657–672 (2011).
52. V. Vajda, A. Ocampo, E. Ferrow, C. Bender-Koch, Nano particles as the primary cause for long-term sunlight suppression at high southern latitudes following the Chicxulub impact—evidence from ejecta deposits in Belize and Mexico. *Gondwana Res.* **27**, 1079–1088 (2015).
53. R. S. Lewis, E. Anders, E. Anders, Cretaceous extinctions: Evidence for wildfires and search for meteoritic material. *Science* **230**, 167–170 (1985).
54. H. J. Melosh, N. M. Schneider, K. J. Zahnle, D. Latham, Ignition of global wildfires at the Cretaceous/Tertiary boundary. *Nature* **343**, 251–254 (1990).
55. O. B. Toon, K. Zahnle, D. Morrison, R. P. Turco, C. Covey, Environmental perturbations caused by the impacts of asteroids and comets. *Rev. Geophys.* **35**, 41–78 (1997).
56. D. A. Kring, D. D. Durda, Trajectories and distribution of material ejected from the Chicxulub impact crater: Implications for postimpact wildfires. *J. Geophys. Res. Planets* **107**, 6–22 (2002).
57. D. D. Durda, D. A. Kring, Ignition threshold for impact-generated fires. *J. Geophys. Res. Planets* **109**, E08004 (2004).
58. J. Morgan, N. Artemieva, T. Goldin, Revisiting wildfires at the K-Pg boundary. *J. Geophys. Res.* **118**, 1508–1520 (2013).
59. C. G. Bardeen, R. R. Garcia, O. B. Toon, A. J. Conley, On transient climate change at the Cretaceous-Paleogene boundary due to atmospheric soot injections. *Proc. Natl. Acad. Sci. U.S.A.* **114**, E7415–E7424 (2017).
60. Gulick *et al.*, "Expedition 364 methods. Chicxulub: Drilling the K-Pg impact crater" in *Proceedings of the International Ocean Discovery Program*, J. Morgan, S. Gulick, C. L. Mellett, S. L. Green; Expedition 364 Scientists, Eds. (International Ocean Discovery Program, College Station, TX, 2017), vol. 364.
61. C. M. Lowery *et al.*, Rapid recovery of life at ground zero of the end-Cretaceous mass extinction. *Nature* **558**, 288–291 (2018).
62. J. Hjulstrom, "Transportation of detritus by moving water" in *Recent Marine Sediments*, P. D. Trask, Ed. (The Society of Economic Paleontologists and Mineralogists Recent Marine Sediments, Broken Arrow, OK, 1955), vol. 4.
63. L. Marynowski, B. R. Simoneit, Widespread upper triassic to lower jurassic wildfire records from Poland: Evidence from charcoal and pyrolytic polycyclic aromatic hydrocarbons. *Palaios* **24**, 785–798 (2009).
64. E. H. Denis *et al.*, Polycyclic aromatic hydrocarbons (PAHs) in lake sediments record historic fire events: Validation using HPLC-fluorescence detection. *Org. Geochem.* **45**, 7–17 (2012).
65. A. T. Karp, A. K. Behrensmeyer, K. H. Freeman, Grassland fire ecology has roots in the late Miocene. *Proc. Natl. Acad. Sci. U.S.A.* **115**, 12130–12135 (2018).
66. K. Grice *et al.*, New insights into the origin of perylene in geological samples. *Geochim. Cosmochim. Acta* **73**, 6531–6543 (2009).
67. A. Kowitz *et al.*, Revision and recalibration of existing shock classifications for quartzose rocks using low-shock pressure (2.5–20 GPa) recovery experiments and mesoscale numerical modeling. *Meteorit. Planet. Sci.* **51**, 1741–176 (2016).
68. S. C. Gupta, T. J. Ahrens, W. Yang, Shock-induced vaporization of anhydrite and global cooling from the K/T impact. *Earth Planet. Sci. Lett.* **188**, 399–412 (2001).
69. C. Prescher, F. Langenhorst, U. Hornemann, A. Deutsch, Shock experiments on anhydrite and new constraints on the impact-induced SO<sub>x</sub> release at the K-Pg boundary. *Meteorit. Planet. Sci.* **46**, 1619–1629 (2011).
70. E. J. Liu, K. V. Cashman, A. C. Rust, S. R. Gislason, The role of bubbles in generating fine ash during hydromagmatic eruptions. *Geology* **43**, 239–242 (2015).
71. G. S. Collins *et al.*, Dynamic modeling suggests terrace zone asymmetry in the Chicxulub crater is caused by target heterogeneity. *Earth Planet. Sci. Lett.* **270**, 221–230 (2008).
72. R. A. DePalma *et al.*, A seismically induced onshore surge deposit at the KPg boundary, North Dakota. *Proc. Natl. Acad. Sci. U.S.A.* **116**, 8190–8199 (2019).
73. V. V. Shuvalov, N. A. Artemieva, "Atmospheric erosion and radiation impulse induced by impacts" in *Catastrophic Events and Mass Extinctions: Impacts and Beyond*, C. Koeberl, K. G. MacLeod, Eds. (Geological Society of America Special Paper, Denver, CO 2002), vol. 356, pp. 695–703.
74. C. M. Belcher *et al.*, An experimental assessment of the ignition of forest fuels by the thermal pulse generated by the Cretaceous–Palaeogene impact at Chicxulub. *J. Geol. Soc. London* **172**, 175–185 (2015).
75. N. J. de Winter, P. Claeys, Micro X-ray fluorescence ( $\mu$  XRF) line scanning on Cretaceous rudist bivalves: A new method for reproducible trace element profiles in bivalve calcite. *Sedimentology* **64**, 231–251 (2017).
76. B. Hall *et al.*, Dual energy CT-scanning and processing of core from the peak ring of the Chicxulub impact structure: Results from IODP-ICDP Expedition 364. Presented at the 48th Lunar and Planetary Science Conference, The Woodlands, Texas, 20 to 24 March 2017 (Abstract 1697) (2017). <https://www.hou.usra.edu/meetings/lpsc2017/pdf/1697.pdf>. Accessed 9 December 2017.
77. S. Siddiqui, A. A. Khamees, "Dual energy CT-scanning applications in rock characterization" in *Proceedings of the SPE Annual Technical Conference and Exhibition* (2004).
78. E. Sturkell, J. Örmö, A. Lepinette, Early modification stage (preresurge) sediment mobilization in the Lockne concentric, marine-target crater, Sweden. *Meteorit. Planet. Sci.* **48**, 321–338 (2013).
79. J. Mazzullo, A. G. Graham, C. Braunstein, *Handbook for Shipboard Sedimentologists* (Ocean Drilling Program, College Station, TX, 1988).
80. K. Simonyan, A. Zisserman, Very deep convolutional networks for large-scale image recognition. arXiv:1409.1556 (4 September 2014).
81. B. Hariharan, P. Arbelaez, R. Girshick, J. Malik, "Hypercolumns for object segmentation and fine-grained localization" in *Proceedings of the IEEE Conference on Computer Vision and Pattern Recognition*, (IEEE, 2015), pp. 447–456.
82. T. Chen, C. Guestrin, "XGBoost: A scalable tree boosting system" in *Proceedings of the 22nd ACM SIGKDD International Conference on Knowledge Discovery and Data Mining*, B. Krishnapuram, Ed. (Association for Computing Machinery, New York, NY, 2016), pp. 785–794.
83. P. Krähenbühl, V. Koltun, Efficient inference in fully connected CRFs with Gaussian edge potentials. *Adv. Neural Inf. Process. Syst.* **24**, 109–117 (2011).
84. S. van der Walt *et al.*; scikit-image contributors, scikit-image: Image processing in Python. *PeerJ* **2**, e453 (2014).
85. J. L. Kirschvink, The least-squares line and plane and the analysis of palaeomagnetic data. *Geophys. J. R. Astron. Soc.* **62**, 699–718 (1980).
86. J. J. Stoker, *Water Waves. The Mathematical Theory with Applications* (Interscience Publ, New York, 1957).
87. K. Grice, B. Nabbefeld, E. Maslen, Source and significance of selected polycyclic aromatic hydrocarbons in sediments (Hovea-3 well, Perth Basin, Western Australia) spanning the Permian-Triassic boundary. *Org. Geochem.* **38**, 1795–1803 (2007).